Article

A Facile Fabrication of PA12/CNTs Nanocomposites with Enhanced Three-Dimensional Segregated Conductive Networks and Electromagnetic Interference Shielding Property through Selective Laser Sintering

Yu Xiong, Haoran Pei, Qinniu Lv, and Yinghong Chen*

Read Online

ACCESS | Metrics & More | Article Recommendations | SI Supporting Information

ABSTRACT: The material design could be very critical in the preparation of conductive polymer composites for electromagnetic interference (EMI) shielding applications. In this work, two methods were proposed to prepare PA12 composite powders coated with CNTs, including ball-milling (BM) and ultrasonic dispersion-liquid phase deposition strategies. Then, by applying selective laser sintering printing (SLS) 3D printing, the segregated network structures were successfully constructed. Various characterization techniques were employed to validate the presence of the formed segregated network structure in the SLS 3D printed parts. The BM SLS 3D printed part at a loading of 5.66 wt % CNTs exhibited an optimum electrical conductivity of 3.0 S/m and an electromagnetic interference shielding (EMI SE) of 23.9 dB (2.0 mm thickness), while its electrical percolation threshold was found to be at 0.347 wt %. However, the EMI SE values of homogenous PA12/CNTs composites prepared by the melt compounding-cryogenic pulverization (MP) method and melt compounding-compression molding were only 9.8 and 15.6 dB, respectively. In addition, the incorporation of CNTs decreased the mechanical performance of the PA12/CNTs printed part due to their negative effect on the sintering. However, such a decrease could be inhibited by increasing the laser energy density. The related investigation could offer a solution to the preparation of the conductive polymer composite and the EMI shielded material through SLS 3D printing processing.
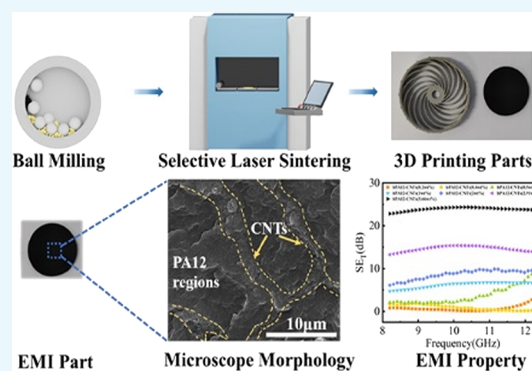
1. INTRODUCTION

The widespread use of electronic devices generates a great plenty of electromagnetic radiations, which would cause interference in the operation of precision electronic equipment and harmfully affect the living environment for human beings.[1−3] Many efforts have been made for the development of electromagnetic interference (EMI) shielding materials to reduce or eliminate the negative effects of the electromagnetic radiations.[4−9] The conductive polymer composites (CPCs), which are fabricated by compositing a polymer matrix with conductive fillers, have attracted many interests for EMI shielding applications owing to their advantageous characteristics, such as low density, corrosion resistance, and ease of processing.[10,11] Nevertheless, the high EMI shielding property of one material generally requires a high loading of conductive fillers, and this simultaneously means a cost increase and processability deterioration.[12] Therefore, preparing CPCs at low filler loadings has still remained as a challenge. The recent studies indicate that the EMI shielding property is not only dependent on the filler type and filler content but also related to the polymer composite structure.[13−16] In the polymer-based EMI shielding composites, there are various filler structures

reported, such as a homogenous structure, segregated structure, porous structure, and layered structure.[3,17] Among the different polymer composite structures, it is recognized that the construction of segregated structures has been considered as an effective way to obtain the high electrical conductivity even at a low content of conductive fillers for CPCs. Sun et al. reported a very high conductivity of 1081 S/m in a segregated MXene/PS composite with only 1.9 vol % MXene.[18] However, the high viscosity of the polymer matrix is required to prevent the diffusion of nanofillers because of the high-pressure during compression molding. Additionally, the compression molding method is only suitable for fabricating some simple products.[19]
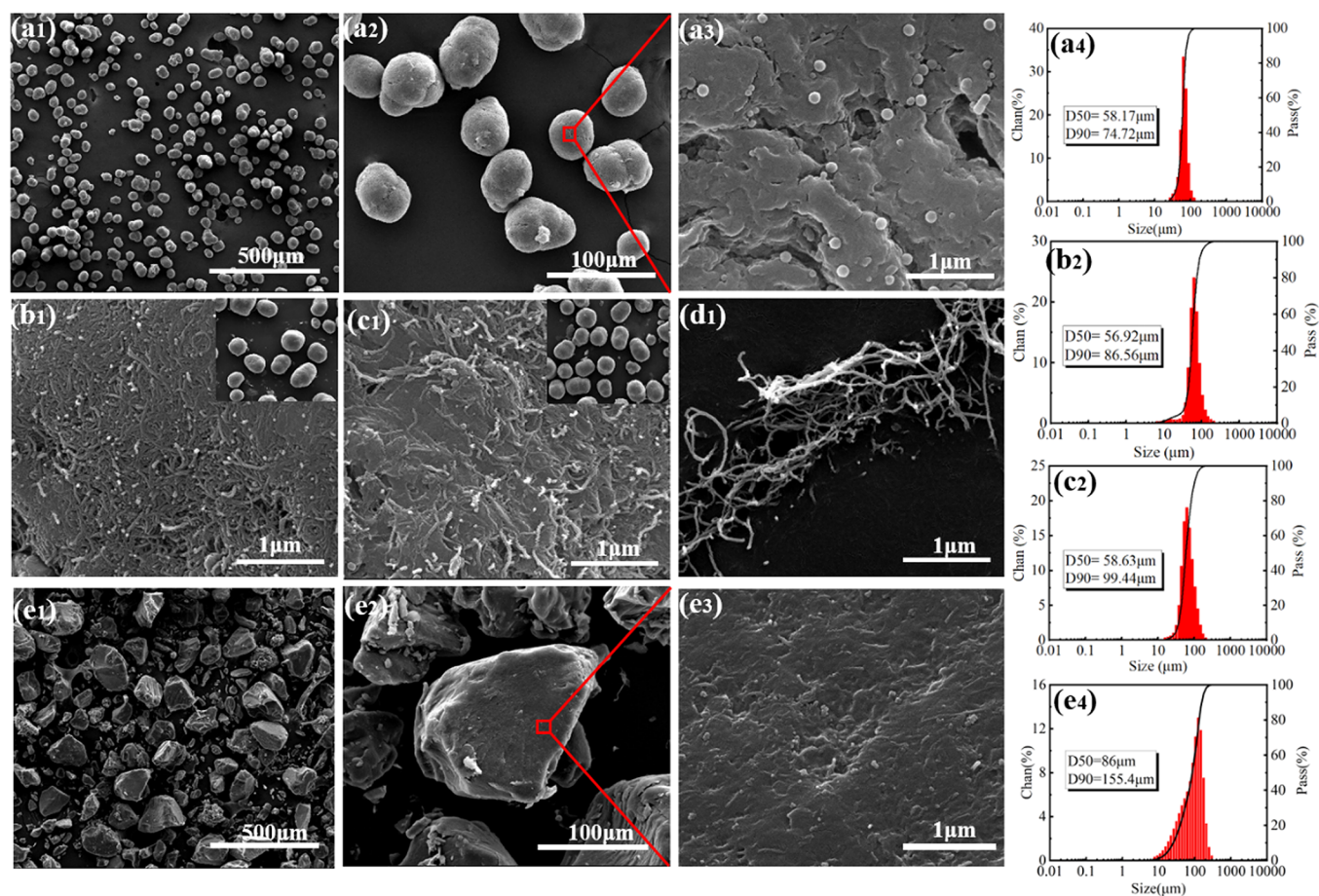
Selective laser sintering (SLS) is one of 3D printing technologies based on the powder system, which employs a

Figure 1. SEM images of different powders at different magnifications and their particle size distribution: pristine pure PA12 powder (a1−a4), bPA12-CNTs (5.66 wt %) (b1−b2), uPA12-CNTs (5.66 wt %) (c1−c2), pristine CNTs (d1), and mPA12-CNTs (5.66 wt %) (e1−e4).

CO_2 laser as the heat source to melt and bind powder particles.[20−24] During such an SLS 3D printing process, the original structure of powders could be maintained to a considerable degree. Obviously, the above prominent and distinctive characteristics proposed a novel idea for constructing the segregated structures and hereby fabricating the CPCs.[25] The key advantages of the SLS 3D printing over the other additive manufacturing techniques and traditional processing methods are in a near zero-shear-rate layer-by-layer fabrication process and also the higher precision and the greater freedom degree for design and fabrication.[26] For example, the injection molding and compression molding methods cannot consistently maintain the segregated structure, and it is difficult for them to manufacture parts with a complex structure.[27] Hence, the SLS technology is one of the most promising technologies for preparation of CPCs and the key influencing factor is in the preparation of suitable powder particles. Mahmoodi et al. investigated the volume resistivity and the electromagnetic interference (EMI) shielding effectiveness (SE) of the injection-molded MWCNT/PS composites, and a low EMI SE of 11.5 dB was exhibited at 5 wt % CNT loading.[28]

In this present study, our emphasis was just focused on preparing PA12 powders coated with CNTs and constructing the networks in the PA12/CNTs composites by applying the sintering process. One method of preparing PA12/CNTs powders is the combination of the ultrasonic dispersion and liquid phase deposition (UDLD) method; the other is the ball-

milling (BM) method. For convenience of comparison, the composite powders with the uniform dispersion of CNTs in the PA12 matrix were prepared by the combination of melt-compounding and the cryogenic pulverization method (MP), and these powders were used to fabricate products by SLS. At the same time, PA12/CNTs nanocomposite parts were also prepared by adopting the traditional melt compounding−compression molding method. To the best of our knowledge, there has been no such similar idea reported for the fabrication of the conductive and EMI PA12/CNTs parts by realizing the segregated conductive network structures using SLS technology. The effects of different preparation methods on the distribution of CNTs, the properties of composite powders, and the performance of 3D printed parts were systematically investigated. In particular, the electrical conductive property, electromagnetic shielding property, and mechanical property of the prepared PA12/CNTs nanocomposite parts were carefully evaluated. The related mechanisms for the three-dimensional conductive network formation and the electromagnetic shielding were also discussed and analyzed.

2. RESULTS AND DISCUSSION

2.1. Characterization of the PA12/CNTs Composite Powders. The parameters of laser sintering and the performance of the sintered part depend on the powder quality and structure[29,30] to a considerable degree. In this study, we adopted two methods to prepare CNT coating PA12 composite powders (UDLD and BM methods). For the
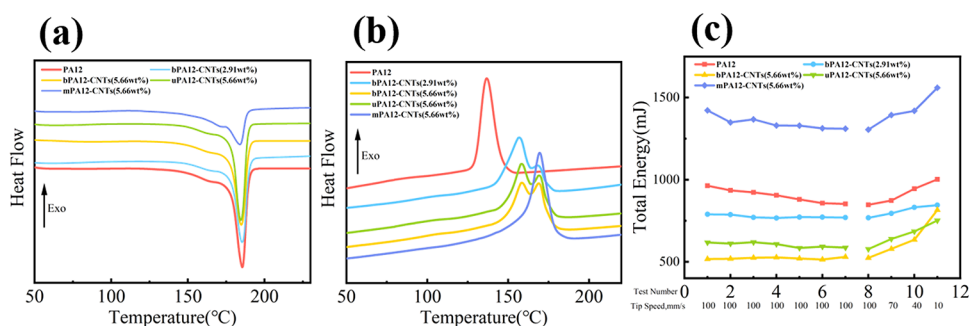
Figure 2. DSC heating (a) and cooling (b) curves; the flow energy test results at fixed and varying tip speed (c). The red line (dotted) represents pristine PA12; the blue line (dotted) represents the bPA12-CNTs (2.91 wt %) powders; the yellow line (dotted) represents the bPA12-CNTs (5.66 wt %) powders; the green line (dotted) represents the uPA12-CNTs (5.66 wt %) powders; the purple line (dotted) represents the mPA12-CNTs (5.66 wt %) powders.

UDLD method, the continuous ultrasonic treatment would make CNTs disperse homogeneously in ethanol, and the obtained CNT suspension was in an opaque liquid state. After adding PA12 powders, the PA12 powders as well as the CNTs filler particles were quickly completely precipitated at the bottom of the beaker. It is believed that the CNT particles are mostly deposited on the surface of PA12 particles during precipitation. On the other hand, for the BM method, the CNT particles were coated on the surface of PA12 particles under the effect of very strong impact and shear force during ball milling. The ball milling with a 350 rpm medium speed and 1 h treatment can ensure that there is enough time and shear force to make the CNTs be encapsulated on the surface of the PA12 particles. Obviously, both UDLD and BM methods could be used to realize the effective distribution of CNT particles on the surface of polymer powder particles, thus forming an encapsulation morphology with CNTs being coated on the polymer particle surface, which has been confirmed by the SEM morphology observation (Figure 1). The pristine pure PA12 powder particles are in an ellipsoid, and the surface is smooth, while the surface of PA12/CNTs composite powder particles prepared by BM and UDLD methods is obviously rough. The interfacial interactions between CNTs and the PA12 matrix were investigated using FT-IR characterization. The results and analyses are presented in the Supporting Information (Figure S1). It can be known that there are the strong interfacial molecular interactions (hydrogen bonding) between the incorporated CNTs and PA12. Actually, for the BM method, the continuous impact and shear forces would make CNTs closely adhere to the surface of PA12 particles, and the involved interfacial interactions are much stronger, as also seen from Figure S1 (more blue shift). Therefore, both ultrasonic dispersion and ball-milling strategies would not only make CNTs encapsulated on the PA12 powder particles but also avoid the CNT agglomeration. It is also noted that the particle size distributions of pristine PA12, bPA12-CNTs, and uPA12-CNTs particles are all narrow. However, for the PA12/CNTs composite powders prepared through the combined melt-compounding and cryogenic pulverization (MP) method, the shape of particles was irregular, and few CNTs can be observed (Figure 1e1−e3). The CNT fillers are mostly embedded into the particles and only some white points could be observed, which are caused by the cross section of the CNTs on the surface. The melt-compounding method could achieve the uniform dispersion of CNTs in the polymer matrix. The

obtained PA12/CNTs composite was further cryogenically pulverized into powder particles (mPA12-CNTs) suitable for SLS 3D printing. There is a significant difference between the pristine pure PA12 and the mPA12-CNTs composite powders in the size and size distribution (Table S1). Compared with pure PA12, the particle size of mPA12-CNTs composite powders is relatively bigger, and their particle size distribution is also broader. This indicates that the prepared mPA12-CNTs composite powders may have a relatively poorer SLS 3D printing processability, as would be investigated later.

During SLS processing, the temperature difference between the initial melting temperature (T_{im}) and initial crystallization temperature (T_{ic}) is defined as the SLS sintering window, which could be determined by the DSC measurement.[31] From the DSC melting curves (Figure 2a) and the DSC data (Table S2), it is seen that the melting temperature of composite powders prepared by different methods does not change obviously. In addition, the melting peak area (melting enthalpy) of mPA12-CNTs is remarkably lower than that of the other CNTs containing PA12 samples. The reason for this is possibly related to the melt-extrusion processing of the mPA12-CNTs composite before its pulverization. During the extrusion process, the matrix PA12 has experienced a very rapid cooling crystallization process to form the PA12/CNTs composite. Therefore, the PA12 macromolecular chains can hardly have enough time to rearrange and crystallize, resulting in a decrease of crystallinity. Moreover, the movement of the PA12 macromolecular chains was also possibly restricted by the well-dispersed CNTs, leading to reduction in the crystallinity. The above two reasons can well explain that the melting enthalpy of mPA12-CNTs composite powder was less than that of the PA12, bPA12-CNTs, and uPA12-CNTs powders.

Also, from the cooling curves of different samples (Figure 2b), it is noted that there is a more obvious difference in the cooling crystallization process and the results are particularly interesting. Compared with pure PA12, the crystallization temperature of all the CNTs containing composite powders significantly increases (particularly for mPA12-CNTs, the temperature difference reaches 32.6 °C), indicating that the incorporated CNTs nanofillers have a remarkable heterogeneous nucleation effect on the crystallization of PA12 as the nano nucleating agent. Also, it is noted that there is a bimodal distribution in the crystallization curves of the composite powder samples with CNTs being coated on the surface of PA12 particles (for bPA12-CNTs and uPA12-CNTs only).

This is a very interesting phenomenon, which was found by us for the first time. This is exactly caused by the difference in the CNT distribution. For the mPA12-CNTs composite powder, the CNTs are homogeneously dispersed in the PA12 matrix (only one structure here). During the DSC heating and cooling process, the influence of the incorporated CNTs on the PA12 crystallization would be consistent, thus resulting in one crystallization peak with much higher temperature than that of pure PA12 due to the heterogeneous nucleation effect of CNTs. However, for bPA12-CNTs and uPA12-CNTs composite powders, the CNTs are encapsulated on the surface of the PA12 powder particle. Actually, there are two structures in the coated PA12 particle. One is the skin layer of CNTs coating PA12 and the other is the matrix PA12 core layer. As a result, during the DSC cooling stage, the cooling just starts from the external layer of the melting coated PA12 particle and then occurs on its core layer. Obviously, due to the remarkable heterogeneous nucleation effect of CNTs, the skin layer of CNT coating PA12 would crystallize first, resulting in the appearance of the first high-temperature crystallization peak (as mPA12-CNTs does). Then, when the temperature further cools down, the underlying matrix PA12 core layer with almost no CNTs would crystallize again, resulting in appearance of the second low-temperature crystallization peak. In addition, it is also noted that, for the bPA12-CNTs sample, with increasing the CNTs loading, the intensity of the high-temperature crystallization peak increases and the intensity of the low-temperature crystallization peak decreases. This is possibly because the increasing amount of CNTs coating could make more of the PA12 macromolecular chains be crystallized under their heterogeneous nucleation effect, and at the same time, the content of the matrix PA12 core layer for each coated PA12 particle (per unit weight) decreases and accordingly, less amount of PA12 macromolecular chains could be crystallized. In addition, relative to bPA12-CNTs, uPA12-CNTs composite powders have the higher low-temperature crystallization peak intensity and, however, possess the lower high-temperature crystallization peak intensity. This indirectly indicates that the ball-milling could more efficiently realize the coating of CNTs on PA12 powder particles than the ultrasonication. In order to further investigate the crystal structure and crystallization behavior of PA12/CNTs 3D printed parts, the X-ray diffraction (XRD) characterization was also conducted. The results and corresponding discussions are supplemented in the Supporting Information (Figure S2 and Table S3).

The dynamic powder flowability is another important parameter for SLS 3D printing.[32] Here, the FT4 powder rheometer was applied to evaluate the flow kinetics and stability of the powder. The FS 3300 PA12 powder particles prepared through the solvent precipitation process are in an ellipsoid-like shape and hence exhibit good flowability. As indicated in Figure 2c, the coating of CNTs on the surface of PA12 powder particles remarkably decreases the BFE value (bPA12-CNTs and uPA12-CNTs), indicating that the flowability of PA12-CNTs powder is significantly improved. This is beneficial to the powder spreading process. In addition, for the bPA12-CNTs composite powder, with increasing the CNT loading, the BFE value decreases. This reveals that the increase in the amount of the coated CNTs would also enhance the powder flowability. The reason for this is that the coated CNTs, which act as the nano-flow modifier, could reduce the friction between powder particles. Furthermore, the BFE value of bPA12-CNTs is lower than that of uPA12-CNTs.

This means that the bPA12-CNTs composite powders have the better flowability than the uPA12-CNTs ones, which again indirectly indicates that the ball milling really exhibits the higher efficiency in the coating of CNTs on the surface of PA12 particles than the ultrasonication. From Figure 2c, it is also noted that the mPA12-CNTs composite powder shows the highest BFE value among all the samples, indicating its poorest flowability and hence the poor 3D printing processability, possibly due to their irregular particle shape. This would result in difficulty in spreading of powders and the poor surface precision of 3D printed parts.

2.2. Electrical Property of PA12/CNTs SLS 3D Printed Parts. The electrical property of different SLS 3D printed parts was investigated by using the broadband dielectric spectrometer (Agilent HP4294A system) in the frequency range of 1 Hz−10 MHz. The measurement of the electrical conductivity at different frequencies could be used to evaluate the formation of electrical conductive networks of one material. Generally speaking, if the electrical conductivity does not change with the frequency, there is the complete electrical conductive networks formed in the prepared parts. Otherwise, if the electrical conductivity depends on the frequency, this means that there is no the complete electric conductive networks formed in the prepared parts.[33] It is worth noting that the electrical conductivity of different frequencies is always lower than the electrical conductivity without frequency change. Therefore, considering the practical applications, the electrical conductivity without frequency change was also tested using a four-point probe instrument to calculate the electrical conductive percolation threshold. The results are shown in Figure 3. As can be seen, the incorporation of CNTs remarkably enhances the electrical conductivity of pure PA12. In addition, the SLS 3D parts printed from the bPA12-CNTs and uPA12-CNTs composite powders with the CNT coating structure exhibit the higher electrical conductivity than the mPA12-CNTs 3D printed part. This adequately indicates that the CNT coating structure (bPA12-CNTs and uPA12-CNTs) could improve the electrical conductivity more effectively than the uniformly dispersed CNTs (mPA12-CNTs). In order to determine the electrical conductive percolation threshold in bPA12-CNTs parts, the composite powders with different CNT contents (0.2−5.66 wt %) were prepared, and the electrical conductivity of the corresponding 3D printed parts was measured (Figure 3b). It can be seen that an abrupt increase in electrical conductivity was observed for the part with 0.4 wt % CNT loading. According to the classical percolation theory, the electrical conductive percolation threshold (x_c) follows a power law relationship as shown in eq 1.

$$\sigma \propto (x - x_c)^{\alpha} \tag{1}$$

where σ is the experimental electrical conductivity for mass fraction $x > x_c$ and α is the critical exponent. After calculation, the electrical conductive percolation threshold of bPA12-CNTs part is only 0.347 wt %. The encouraging result of the above low percolation threshold could be attributed to the no molding pressure and the near-zero-shear-rate occurring during the layer-by-layer SLS 3D printing fabrication, which can preserve the original powder structure (CNT coating PA12 particles) to the greatest extent. As seen from Figure 3c, for pure PA12, at the very low frequency, the electrical conductivity is only 10^{-11} S/m and obviously exhibits frequency dependence (constantly increases with the fre-
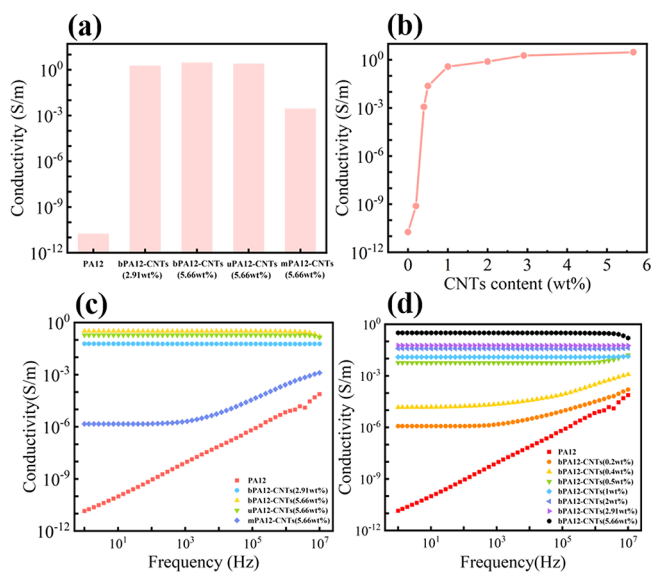
Figure 3. Electrical conductivity of different samples: pure PA12, bPA12-CNTs (2.91 wt %), bPA12-CNTs (5.66 wt %), uPA12-CNTs (5.66 wt %), and mPA12-CNTs (5.66 wt %) (a), bPA12-CNTs with different CNT loadings (b), PA12/CNTs 3D printed parts prepared from different composite powders at different frequencies (c) (the red square represents pristine PA12; the blue circle represent the bPA12-CNTs (2.91 wt %); the yellow triangle represents the bPA12-CNTs (5.66 wt %); the green triangle represents the uPA12-CNTs (5.66 wt %); the purple diamond represents the mPA12-CNTs (5.66 wt %)); bPA12-CNTs 3D printed parts with different CNT loadings at different frequencies (d) (the red square represents pristine PA12; the orange circle represents bPA12-CNTs (0.2 wt %); the yellow triangle represents bPA12-CNTs (0.4 wt %); the green triangle represents bPA12-CNTs (0.5 wt %); the blue diamond represents bPA12-CNTs (1 wt %); the indigo triangle represents bPA12-CNTs (2 wt %); the purple triangle represents bPA12-CNTs (2.91 wt %); the black circle represents bPA12-CNTs (5.66 wt %)).

quency). Moreover, for the mPA12-CNTs 3D printed parts, the electrical conductivity varies little in the low frequency range and, however, obviously increases with the frequency in the high frequency range, also showing the frequency dependence. Above results show that in the mPA12-CNTs SLS 3D printed part, there is no formation of the complete electrical conductive networks. This is because it is difficult to form the electrical conductive networks under the SLS 3D printing conditions.[26] However, for bPA12-CNTs and uPA12-CNTs SLS 3D printed parts, the electrical conductivity is remarkably higher than that of the mPA12-CNTs part (about 3 orders of magnitude higher). In the full test frequency range (1−10 MHz), the measured electrical conductivity is stable and does not exhibit the frequency dependence. The above results show that in the bPA12-CNTs and uPA12-CNTs SLS 3D printed parts, the formed electrical conductive networks are relatively perfect. Figure 3d shows the electrical conductivity of the bPA12-CNTs 3D printed parts with different CNT loadings (0.2−5.66 wt %). As can be seen, at 0.4 wt % CNT loading or lower, the electrical conductivity of the 3D printed part shows the frequency dependence and, however, does not have this at 0.5 wt % CNT loading or higher. This result shows that at near 0.4 wt % CNT loading (critical value), there is possibly the perfect electrical conductive networks initially formed, which is consistent with the electrical conductive percolation threshold revealed in Figure 3b. The best electrical

conductivity of the SLS 3D printed PA12/CNTs nano-composite part could reach as high as near 3.0 S/m.

2.3. EMI Shielding Property of PA12/CNTs SLS 3D Printed Parts. Figure 4a illustrates the EMI shielding
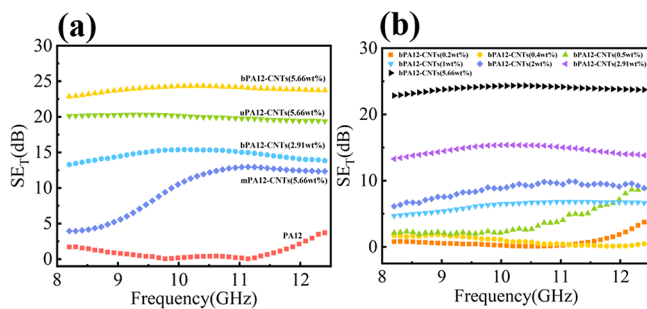
Figure 4. EMI SE_T value of different SLS 3D printed samples at different frequencies (a) (the red square represents pristine PA12; the blue circle represents the bPA12-CNTs (2.91 wt %); the yellow triangle represents the bPA12-CNTs (5.66 wt %); the green triangle represents the uPA12-CNTs (5.66 wt %); the purple diamond represents the mPA12-CNTs (5.66 wt %)); EMI SE_T value of bPA12-CNTs 3D printed parts with different CNT contents (b) (the red square represents pristine PA12; the orange circle represents bPA12-CNTs (0.2 wt %); the yellow triangle represents bPA12-CNTs (0.4 wt %); the green triangle represents bPA12-CNTs (0.5 wt %); the blue diamond represents bPA12-CNTs (1 wt %); the indigo triangle represents bPA12-CNTs (2 wt %); the purple triangle represents bPA12-CNTs (2.91 wt %); the black circle represents bPA12-CNTs (5.66 wt %)).

property of the PA12/CNTs nanocomposite SLS 3D printed parts in the range of X-band (8.2−12.4GHz).[34,35] It can be seen that the EMI shielding effectiveness (SE) values of most 3D printed samples exhibit a weak frequency dependence in the full test frequency range and only for the mPA12-CNTs 3D printed sample, the EMI SE value presents an increasing tendency with frequency in the middle test frequency range (8.5−11.0 GHz). For the bPA12-CNTs 3D printed parts, the increase of CNT loading could significantly enhance the EMI shielding property (from about 14.6 to 23.9 dB). In addition, at the same CNT loading, the bPA12-CNTs and uPA12-CNTs SLS 3D printed parts show the much better electromagnetic shielding performance than the mPA12-CNTs one. Moreover, the bPA12-CNTs sample also presents the obviously higher EMI SE value than the uPA12-CNTs sample, exhibiting the advantage of the ball-milling strategy. It is known that the commercial application standard of the EMI shielding materials is at an EMI SE of 20 dB, where 99% incident EM waves could be absorbed and reflected through the shielding materials. Obviously, at 5.66 wt % CNT loading, the obtained bPA12-CNTs and uPA12-CNTs 3D printed parts with EMI SE values of 23.91 and 19.95 dB, respectively, could satisfy the requirements for practical application. From the following eq 2, the value for blocking EM irradiation can be calculated.

$$SE_T(dB) = 10lg(Pi/Pt) \qquad (2)$$

where Pi is the incident power and Pt is the transmitted power in decibel (dB). The calculation demonstrates that only 0.40% of EM irradiation could be transmitted for the bPA12-CNTs part with 5.66 wt % CNTs.

Figure 4b shows the influence of CNT loading on the EMI SE of the bPA12-CNTs 3D printed part. It can be seen that, with increasing the CNT loading, the EMI SE basically exhibits

an increasing tendency. Particularly, when the CNT loading is more than 2.0 wt %, the corresponding EMI SE increases remarkably, revealing a greatly attractive and large potential application. Considering the porosity of the SLS 3D printed part, here, the thickness normalized specific SE value (SSE/t, SE divided by the sample density and thickness)[19] was also used to characterize the electromagnetic shielding performance of the 3D printed parts, which can indirectly reflect the influence of density and porosity. Accordingly, the influence of different powder fabrication methods and CNT contents on the SSE/t of PA12/CNTs SLS 3D printed part was investigated. The results are shown in Figure S3. As can be seen, the bPA12-CNTs (5.66 wt %) part shows the optimum SSE/t. The SSE/t of PA12/CNTs 3D printed parts from the different powder fabrication method decreases in the order of ball-milling > ultrasonic treatment > melt-compounding. For ball-milling, the increase of CNT loading would remarkably enhance the SSE/t. Evidently, the combination of ball-milling and the SLS 3D printing strategy shows a certain advantage in preparation of the EMI shielded part.

2.4. Electrical Conductive Network Construction and Electromagnetic Shielding Mechanism.

In order to verify that the significant improvements in electrical conductivity and EMI SE of the PA12/CNTs nanocomposite 3D printed part are mainly caused by the construction of the perfect electrical conductive networks, which is realized by SLS 3D printing of the CNT coating PA12 powder particles, the optical microscopy (OM) observation as well as the SEM characterization was adopted to investigate the formation of the segregated structures. The obtained results are shown in Figure 5 and Figure S4. In the OM images, the light-colored areas are
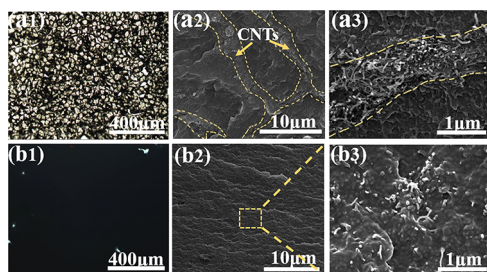

Figure 5. Optical microscopy and SEM photos of the fractured surface of different SLS 3D printed parts: bPA12-CNTs (5.66 wt %) (a) and mPA12-CNTs (5.66 wt %) (b).

representative of the polymer matrix particles, while the dark areas are basically representative of the carbon nanotubes[36] distributed at the interfaces between the matrix particles above mentioned. As can be seen, in the PA12/CNTs nanocomposite 3D printed parts prepared by BM and UDLD methods, respectively, there is a formation of the segregated 3D electrical conductive networks (this will also be verified by the subsequent SEM measurement). For the bPA12-CNTs system, as the CNT loading increases, there are the more electrical conductive networks formed (light-color area decreases and dark area increases). The light-colored area (polymer matrix) is relatively uniform in size and shape, resulting from the narrow particle size distribution of the PA12 polymer powder particles. For the mPA12-CNTs 3D printed parts prepared through the MP method (Figure 5b), the field of view is almost fully dark. This is possibly due to the uniform distribution of CNTs in the PA12 matrix. As a result, it is impossible to

observe the formed electrical conductive path. From the SEM images, the segregated conductive CNT networks and pathways could also be clearly observed. At the interfaces between particles, there are obviously the bright dots with a successive band structure (CNTs agglomerates) in bPA12-CNTs and uPA12-CNTs 3D printed samples, which could really construct the typical segregated structure. By contrast, for the mPA12-CNTs 3D printed sample, there are no similar segregated network structures in the PA12 matrix. As we know, the SLS 3D printing itself belongs to a near zero-shear-rate layer-by-layer fabrication process. So, it can maintain and preserve the original distribution state of CNTs on the powder particle surface during processing to the greatest extent. During SLS 3D printing process, the powder particles are densely assembled. Then, the adjacent powder particles are melted and further bonded after being irradiated by a CO_2 laser, thus forming a sintering neck. The coated CNTs would be naturally filled into the gaps between particles. Obviously, these coated CNTs would negatively affect the melting and bonding of particles to a certain degree. With the sintering of composite powder particles going on, the interconnected strips consisting of CNT agglomerates and layers would be formed between the adjacent particles, thus finally forming the three-dimensional electrical conductive networks. Here, we also compared the construction of a conductive network between SLS 3D printing and melt compounding−compression molding methods. However, the latter has a very high shear force and high molding pressure, while the former has no such pressure and shear force. This shows there are much more perfect conductive segregated networks formed in the 3D printed part than in the compression-molded part (Figure S5), resulting in the much lower EMI shielding property (Figure S6). The details for comparison are provided in the Supporting Information.

Figure 6a1−a4,b clearly illustrates the specific mechanism of EMI shielding. The EMI shielding parameters, including the
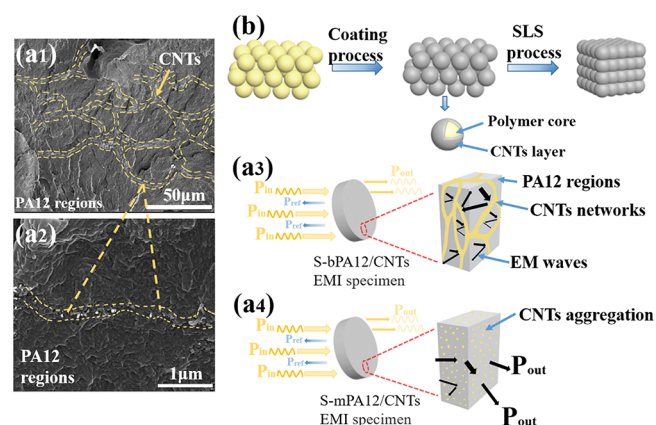
Figure 6. SEM images of the fractured surface of bPA12-CNTs SLS 3D printed part (a1−a2); electromagnetic shielding mechanism for the bPA12-CNTs (a3) and mPA12-CNTs SLS 3D printed parts (a4); schematic illustration for the formation mechanism of the segregated conductive network of the bPA12-CNT system (b).

coefficient absorption power (A), reflection power (R), transmission power (T), total shielding (SE_T), microwave absorption (SE_A), and microwave reflection (SE_R) are shown in Figure S7. According to the literature, SE_R and SE_A can be calculated through eqs 3 and 4:[37,38]

$$SE_R = 168.2 + 10\log\left(\frac{\sigma_r}{f\mu_r}\right) \quad (3)$$

$$SE_A = 131.43t\sqrt{f\mu_r\sigma_r} \quad (4)$$

where σ_r is the relative electrical conductivity, μ_r represents the relative magnetic permeability, f is the frequency of electromagnetic waves, and t represents the thickness of the shielding materials.

Obviously, according to eqs 3 and 4, a part with high conductivity and permeability can shield the EM wave more efficiently.[39] As can be seen from Figure S7, except for mPA12-CNTs, in the other 3D printed samples, the contribution of absorption (SE_A, A) is much larger than that of reflection (SE_R, R), indicating that the involved electromagnetic shielding works mainly based on the absorption-dominant mechanism, which would not cause the secondary pollution and meet the requirements for the low EM reflection value in green environmental protection. However, as far as the mPA12-CNTs 3D printed part is concerned, the reflection (SE_R, R) is higher than the absorption (SE_A, A), reflecting that the involved electromagnetic shielding is mainly controlled by the EM reflection. The reason for this is related to the formation of a conductive network in the system. Comparatively, the more complete conductive network is formed in the bPA12-CNTs parts, which allows the electrons to be efficiently transferred and to dissipate more electric energy. When the EM waves are transmitted to the bPA12-CNTs 3D printed parts, a large fraction of EM waves would enter inside the parts and then be trapped in the 3D conductive segregated CNT networks, while a small part of waves would be reflected back.[40] Because the EM waves can hardly break through the CNT boundaries, the trapped EM waves would be absorbed, reflected, and scattered repeatedly and finally be consumed efficiently by transforming into heat. In comparison, for the mPA12-CNTs 3D printed sample, a less amount of EM waves could be absorbed by the CNTs dispersed in the PA12 matrix, thus resulting in the poor EMI shielding property. All the above results show that the effective combination of the selective laser sintering (no shear stress) and the coating strategies including UDLD and BM can construct and retain the 3D segregated network structures so as to achieve the improvement in electromagnetic shielding performance. By contrast, the traditional melt compounding−pulverization combination method could not build such complete and continuous 3D segregated networks. This is the reason why the mPA12-CNTs 3D printed sample shows the poor EMI shielding performance.

2.5. Mechanical Properties of the PA12-CNTs Nanocomposites. Figure 7a shows the mechanical properties of the 3D printed samples of pure PA12 and PA12/CNTs nanocomposites prepared through different methods. As can be seen, the incorporation of CNTs (compared to pure PA12) and increase of the CNTs loading would equally obviously deteriorate the mechanical performances of the 3D printed sample. This is possibly because the incorporated CNTs influence the sintering of composite powders to a certain degree. In addition, for different preparation methods and at the same CNT loading (5.66 wt %), the mechanical performance of the bPA12-CNTs 3D printed sample is much higher than that of uPA12-CNTs and mPA12-CNTs 3D printed samples (compared with uPA12-CNTs, the tensile stress and Young's modulus of bPA12-CNTs are increased by
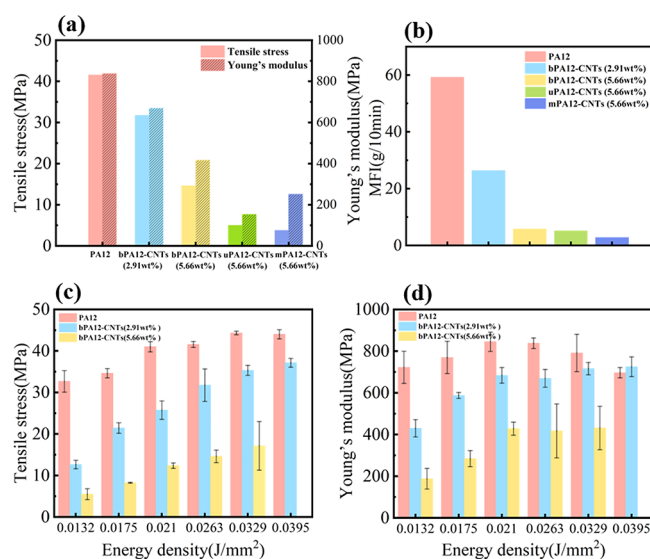

Figure 7. Mechanical performances of the different PA12/CNTs nanocomposite SLS 3D printed parts (a); melt flow index (MFI) of the different PA12/CNTs co-powders (b); tensile stress (c) and Young's modulus (d) of pure PA12, bPA12-CNTs (2.91 wt %) and bPA12-CNTs (5.66 wt %) at different energy densities (the red box represents pristine PA12; the blue box represents the bPA12-CNTs (2.91 wt %); the yellow box represents the bPA12-CNTs (5.66 wt %); the green box represents the uPA12-CNTs (5.66 wt %); the purple box represents the mPA12-CNTs (5.66 wt %)).

193.37 and 172.5%, respectively). The latter two 3D printed samples are actually close (the tensile stress of uPA12-CNTs is relatively higher but its Young's modulus is relatively lower). The reason for this could be that the ball milling can make the coated CNTs more closely combined with the matrix PA12 particles due to its strong impact force and the strongly interacted CNTs at interfaces can more effectively absorb the laser energy, which is helpful for the sintering of PA12 particles.

In order to further understand the reason for the above change, the melt flow index (MFI) test was used to investigate the material sintering and the results are shown in Figure 7b. A SEM instrument was also used to observe the fractured surface of the 3D printed parts, and the results are shown in Figure 8. It can be seen that pure PA12 powder particles are indeed almost completely melted and perfectly sintered due to their high MFI.[41−44] There are a few voids that formed there during the laser sintering (Figure 8a1−a2). Comparatively, a sharp
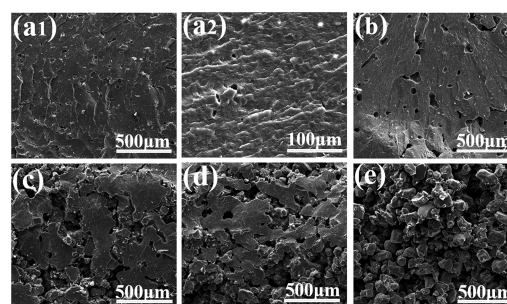
Figure 8. SEM images of the different SLS 3D printed parts: pure PA12 (a1−a2), bPA12-CNTs (2.91 wt %) (b), bPA12-CNTs (5.66 wt %) (c), uPA12-CNTs (5.66 wt %) (d), and mPA12-CNTs (5.66 wt %) (e)
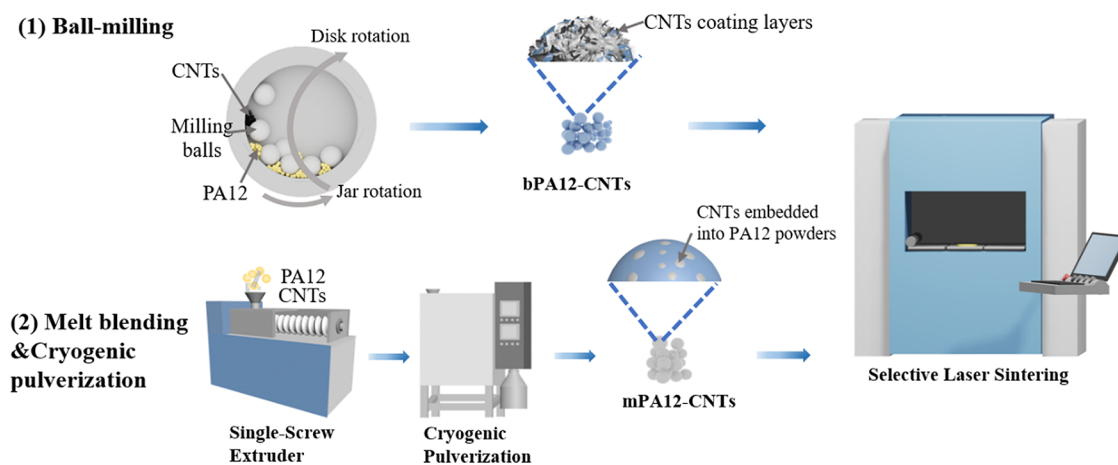
Figure 9. Schematic representation for preparing PA12 co-powders, including ball-milled bPA12-CNTs (1) and melt-compounded mPA12-CNTs (2)

decrease in the MFI value and an increase in the number of matrix holes are observed in PA12/CNTs nanocomposite 3D printed parts (Figure 8b−e). Among all the different 3D printed parts of nanocomposites, the sintering of bPA12-CNTs (2.91 wt %) is the best and the sintering of mPA12-CNTs is the poorest. The reason why the incorporation of CNTs greatly decreases the MFI value of PA12/CNTs nano-composite is explained in the Supporting Information. In addition, the ultrasound-based 3D printed sample also shows the poorer sintering quality than the ball milling 3D printed sample. The morphology changes above mentioned can well explain the changes in mechanical performance of different 3D printed samples. Moreover, we also compared the mechanical properties between SLS 3D printing and melt compounding−compression molding methods. Figure S8 shows that the S-bPA12-CNTs part exhibits the worse mechanical performance than the M-bPA12-CNTs part due to the pores and defects occurring in the former (Figure S5). The details for comparison are provided in the Supporting Information.

As far as SLS 3D printing is concerned, the laser energy density is also a critical factor influencing the mechanical property of 3D printed samples. Figure 7c,d shows the tensile stress and Young's modulus of the 3D printed parts with different energy densities. As can be seen, both tensile strength and Young's modulus of the parts obviously decrease with increasing CNT loading and gradually increase with increasing energy density. This is because when the laser energy density increases, the composite powder particles would have the stronger heat to melt and bond each other to form a sintering neck, thus leading to the enhancement in the mechanical property. At the low energy density, there is insufficient energy for the polymer melt flow and coalescence, thus resulting in more pores in the final parts and a poorer mechanical property. Therefore, the increase of the laser energy density could improve the mechanical performance of 3D printed parts. However, the excessive energy (high energy density) would decrease the mechanical property because the very high energy density would possibly cause the decomposition of the macromolecular chains.[23,45,46] Riedlbauer et al. found that the greater energy density delivered by the laser would result in larger melt pools and thereby the lower dimensional accuracy and deteriorated mechanical property during processing.[47] Actually, the above phenomenon has also appeared in our study, as shown in Figure 7d. At the low energy density, the

physical property of the SLS 3D printed parts increases with increasing laser energy density (0.0132−0.0263 J/mm^2). However, with further increasing laser energy density (to 0.0329 and 0.0395 J/mm^2), the Young's modulus shows a decreasing tendency. This is obviously associated with the material degradation caused by the high laser energy density.

3. CONCLUSIONS

In order to meet the challenge in improving the electrical conductivity and EMI shielding performance of the SLS 3D printed parts, in this work, two strategies, including ball-milling (BM) and combined ultrasonic dispersion and liquid phase deposition (UDLD) methods, were proposed to prepare PA12/CNTs composite powders with CNT coating structure for construction of conductive segregated networks during SLS 3D printing. The formation mechanism was also discussed. As a comparison, the combined melt-compounding and cryogenic pulverization (MP) method was also used to prepare the composite powders with uniformly dispersed CNTs. The results show that the particle size, particle size distribution, and flowability of the composite powders prepared by both BM and UDLD methods equally satisfy the requirement for the SLS 3D printing process, and the coating of CNTs on the surface of PA12 powder particles was realized as expected. The DSC measurement shows that the double peaks in the crystallization curves of the BM and UDLD composite powders are caused by the CNT coating structure on the surface of PA12 particles. The optical microscope and SEM observation indicate that there are complete conductive segregated networks that successfully formed from the coated CNTs at the interfaces in the 3D printed parts of BM (bPA12-CNTs) and UDLD (uPA12-CNTs) methods, respectively, but not in MP 3D printed parts (mPA12-CNTs). Particularly for the bPA12-CNTs system, the electrical conductive percolation threshold could reach as low as 0.347 wt %. In addition, at 5.66 wt % CNTs loading, the electrical conductivity and EMI SE value of the bPA12-CNTs SLS 3D printed part can achieve about 3.0 S/m and 23.9 dB, respectively. Comparatively, the EMI shielding property of the bPA12-CNTs 3D printed part is better than that of the uPA12-CNTs one. Except for the MP 3D printed part, the other BM and UDLD 3D printed parts works mainly based on the absorption-dominant mechanism in electromagnetic shielding. The incorporation of CNTs would deteriorate the mechanical performance of PA12/CNTs 3D

printed parts to a certain degree. However, such an impairment could be compensated by increasing the laser energy density. This study could provide a new strategy and insight for the preparation of the CPCs and electromagnetic shielding parts.

4. MATERIALS AND METHODS

4.1. Materials. Pristine PA12 powders (FS 3300) employed as the polymeric matrix of the composite were purchased from Hunan Farsoon High-Technology Co.,Ltd. Multi-walled carbon nanotubes (MWCNTs, NC7000) with a length of 1.5 μm and an average diameter of 9.5 nm were obtained from Nanocyl S.A., Belgium. Ethanol was provided by Kelong Chemical Reagent Factory (Chengdu, China).

4.2. Preparation of Composite Powders. The schematic diagram for fabrication of PA12/CNTs composite powders (CNT loading: 0.2, 0.4, 0.5, 1, 2, 2.91, and 5.66 wt %) is shown in Figure 9 and Figure S9. For the UDLD method, CNTs were dispersed in ethanol to obtain a homogeneous suspension under mechanical stirring (300 rpm) and ultrasonic treatment for 2 h. Then, PA12 powders were added into the suspension and subjected to mechanical stirring (300 rpm) and ultra-sonication for another 2 h. The CNT coating PA12 composite particles were accordingly prepared after filtering and drying (named uPA12-CNTs powders). For the BM method, the PA12 powders and CNTs were added into a ball milling machine (QM-3SP4, Nanjingnanda Instrument Co., Ltd., China) at a speed of 350 rpm for 1 h to achieve the coating of CNT on the surface of PA12 particles (named bPA12-CNTs powders). As a contrast, the homogeneously dispersed CNT filled PA12 composite powders were also prepared, as follows. First, PA12 powders and pristine CNTs were premixed in a high-speed mixer and then melt-compounded in a single-screw extruder (RM-200C, Harbin HAPRO Electric Technology Co., Ltd., Harbin, China) in the temperature range of 185−210 °C and at a rotation speed of 20 rpm. Finally, the obtained composite extrudates were pulverized using a cryogenic pulverizer (Jiangyin Zhongkai Pharmaceut-ical Machinery Manufacturing Co., Ltd., China) to prepare the composite powders (named mPA12-CNTs powders). The fabrication method and the name of composite powders are resumed in Table 1.

Table 1. The Fabrication Method, Number, and CNT Loading for Various Composite Powders

fabrication method	composite powder	CNT loading (wt %)
ultrasonic dispersion and liquid phase deposition method (UDLD)	uPA12-CNTs	5.66
ball-milling method (BM)	bPA12-CNTs	0.2, 0.4, 0.5, 1, 2, 2.91, 5.66
melt-compounding and cryogenic pulverization method (MP)	mPA12-CNTs	5.66

4.3. Selective Laser Sintering 3D Printing. The 3D printing process was conducted on both pure PA12 and polymer composite powders using an SLS machine equipped with a continuous wave CO_2 laser (HT251P, manufactured by Farsoon Technologies, China). The primary printing param-eters for SLS printing are listed in Table 2, and the other parameters are listed in the Supporting Information (Table S4). The picture of the SLS 3D printed sample is shown in Figure S10. The laser energy density is a function of laser power (LP), scan speed (SS), and scan space (BS). In this study, the scan speed of the SLS machine is 7.6 m/s.

$$\text{eEnergy density(ED)} = \frac{LP}{SS \times BS} \quad (5)$$

4.4. Melt-Compounding and Compression Molding of PA12/CNTs Nanocomposites. As a comparison, PA12/CNTs nanocomposites were prepared using the conventional melt-compounding method. First, bPA12-CNTs (5.66 wt %) particles were directly melt-compounded for 5 min in a banbury mixer at a screw speed of 50 rpm and a temperature of 200 °C. Then, the well-mixed PA12/CNTs nanocomposite pastes were pulverized into pellets. Finally, the obtained pellets were hot-pressed into parts for test at a pressure of 10 MPa and a temperature 200 °C. The hot-pressed bPA12-CNTs nanocomposite part was named as M-bPA12-CNTs. For convenience of comparison, the corresponding SLS 3D printed bPA12-CNTs nanocomposite part was named as S-bPA12-CNTs.

4.5. Characterization. The surface morphologies of pure PA12 and composite powders were observed using a scanning electron microscope (SEM) (FEI, Eindhoven, Netherlands) with an acceleration voltage of 20 kV. The fracture surfaces of the corresponding SLS 3D printed parts were also observed using the above SEM instrument. The samples were cryogeni-cally fractured in liquid nitrogen. All samples were sputtered with gold particles before test.

The size and size distribution of the powders were analyzed on a laser scattering particle size analyzer (Microtrac S3500-SI, USA).

The DSC measurement was carried out using a TA Q20 differential scanning calorimeter analyzer (TA Instruments, USA). The test temperature range was from 40 to 240 °C at a speed of 10 °C/min under a nitrogen atmosphere. All the weight of the sample was 5−10 mg.

The TGA measurement was carried out on a TA Q50 thermogravimetric analyzer (TA Instruments, USA) to determine the actual CNT loading in various PA12/CNTs parts at a heating rate of 10 °C/min under a nitrogen atmosphere with a flow rate of 100 mL/min. The results are shown in Figure S11. The weight of the sample was at 5−10 mg, and the test temperature range was from 30 to 600 °C.

The Fourier transform infrared (FTIR) spectra of PA12 and PA12/CNTs powders were recorded on a Nicolet 6700 FTIR

Table 2. Adopted Parameters for SLS 3D Printing

parameters	values for different condition combination					
scan speed (m/s)	7.6	7.6	7.6	7.6	7.6	7.6
laser power (W)	10	20	40	20	20	30
scan spacing (mm)	0.1	0.15	0.25	0.1	0.08	0.1
energy density (J/mm²)	0.0132	0.0175	0.021	0.0263	0.0329	0.0395

spectrometer (Thermo Fisher Scientific, USA) in a range of 4000−400 cm^{-1}.

X-ray diffraction (XRD) was performed using a DX-1000 diffractometer (Dandong Fangyuan Instrument Co., Ltd., China) to investigate the crystallization of the samples. The Cu Kα generator system was operated at 40 kV and 25 mA, and the 2θ scan ranged from 5 to 60° at a scanning rate of 1°/s.

The flow and accumulation properties of powders were investigated using a Freeman FT4 powder rheometer (Freeman Technology, UK).

The microstructures of the 3D printing parts were observed using an optical microscope (Leica DM2500P, German) to investigate the segregated conductive network of CNTs in the PA12 matrix.

To evaluate the rheological behaviors of the powders, an extrusion plastometer was used to measure the melt flow index (MFI) at 230 °C with 2.16 kg weight.

The electrical property was carried out using an Agilent HP4294A system in the frequency range of 1 Hz−10 MHz. When the conductivity is more than 1×10^{-10} S/m, a four-point probe instrument (RTS-8, Guangzhou Four-Point Probe Technology Co., Ltd., China) was used to record the electrical conductivity of the samples; otherwise, a Picoammeter (Keithley 2400, Keithley Instruments Inc., USA) was used to measure the electrical resistance, which can be converted to electrical conductivity using the following eq 6.

$$\sigma = l/(S \times R) \tag{6}$$

where l is the thickness of samples (m), S is the area of samples (m^2), and R is the measured electrical resistance (Ω). For each sample, three replicates were measured, and the averaged value was used.

The mechanical property was evaluated using a universal material testing machine (Sichuan Dexiang Kechuang Instrument Co.Ltd.) with a cross-head speed of 50 mm/min. Three replicate samples were measured, and the averaged value was adopted.

The Agilent N5247A vector network analyzer was used to evaluate the electromagnetic interference shielding effectiveness (EMI SE) of the samples. All the measured samples have the same dimension of 13 mm diameter and 2 mm thickness. The schematic diagram of the EMI shielding measurement setup is shown in Figure S12. The value of EMI SE is mainly composed of three parts: SE$_A$, SE$_R$, and SE$_M$.[48,49]

$$SE_T = SE_A + SE_R + SE_M \tag{7}$$

In most shielding environments, the SE$_M$ value is very low compared to the other two terms and can be negligible. SE$_A$ and SE$_R$ can be calculated from the power coefficients R (reflection), A (absorption) and T (transmission). For the two-terminal vector network system, the power coefficients R, A, and T can also be obtained according to the S parameters (S_{11}, S_{12}, S_{22}, S_{21}).[50]

$$A + R + T = 1 \tag{8}$$

$$T = |S_{21}|^2 = |S_{12}|^2 \tag{9}$$

$$R = |S_{22}|^2 |S_{11}|^2 \tag{10}$$

$$SE_R = -10\log(1 - R) = -10\log(1 - |S_{22}|^2) \tag{11}$$

$$SE_A = -10\log(T/(1 - R)) = -10\log(|S_{12}|^2/(1 - |S_{22}|^2)) \tag{12}$$

$$SE = SE_A + SE_R = -20\log(|S_{12}|) \tag{13}$$

■ ASSOCIATED CONTENT

ⓢ Supporting Information

The Supporting Information is available free of charge at https://pubs.acs.org/doi/10.1021/acsomega.1c06021.

FTIR result (Figure S1); particle size distribution of different composite powders (Table S1); DSC result (Table S2); XRD result (Figure S2) and the crystallinity at different parameters and thickness (Table S3); specific SE curves (Figure S3); optical microscopy and SEM photos of SLS 3D printed parts (Figure S4); SEM images (Figure S5) and EMI SE$_T$ values (Figure S6) of S-bPA12-CNTs parts and M-bPA12-CNTs parts; SE$_R$, SE$_A$, SE$_T$ values and the coefficients of different parts (Figure S7); mechanical property of S-bPA12-CNTs parts and M-bPA12-CNTs parts (Figure S8); schematic diagram for preparing uPA12-CNTs composite powder (Figure S9); the digital picture for the parts printed by SLS strategy (Figure S10); basic parameters for SLS 3D printing (Table S4); TG result (Figure S11); and schematic description of EMI shielding measurement setup (Figure S12) (PDF)

■ AUTHOR INFORMATION

Corresponding Author

Yinghong Chen − *State Key Laboratory of Polymer Materials Engineering, Polymer Research Institute of Sichuan University, Chengdu 610065, China;* ⓞ orcid.org/0000-0003-2169-4673; Email: johnchen@scu.edu.cn

Authors

Yu Xiong − *State Key Laboratory of Polymer Materials Engineering, Polymer Research Institute of Sichuan University, Chengdu 610065, China*

Haoran Pei − *State Key Laboratory of Polymer Materials Engineering, Polymer Research Institute of Sichuan University, Chengdu 610065, China*

Qinniu Lv − *State Key Laboratory of Polymer Materials Engineering, Polymer Research Institute of Sichuan University, Chengdu 610065, China*

Complete contact information is available at:
https://pubs.acs.org/10.1021/acsomega.1c06021

Notes

The authors declare no competing financial interest.

■ ACKNOWLEDGMENTS

■ REFERENCES

(1) Wang, L.; Ma, Z.; Zhang, Y.; Chen, L.; Cao, D.; Gu, J. Polymer-based EMI shielding composites with 3D conductive networks: A mini-review. *SusMat* **2021**, *1*, 413−431.

(2) Li, J.; Wang, Y.; Yue, T. N.; Gao, Y. N.; Shi, Y. D.; Shen, J. B.; Wu, H.; Wang, M. Robust electromagnetic interference shielding, joule heating, thermal conductivity, and anti-dripping performances of polyoxymethylene with uniform distribution and high content of carbon-based nanofillers. *Compos Sci Technol.* **2021**, *206*, 108681.

(3) Wang, M.; Tang, X. H.; Cai, J. H.; Wu, H.; Shen, J. B.; Guo, S. Y. Construction, mechanism and prospective of conductive polymer composites with multiple interfaces for electromagnetic interference shielding: A review. *Carbon* **2021**, *177*, 377−402.

(4) Kong, D.; Li, J.; Guo, A.; Xiao, X. High temperature electromagnetic shielding shape memory polymer composite. *Chem. Eng. J.* **2020**, *108*, 127365.

(5) Wu, X.; Tu, T.; Dai, Y.; Tang, P.; Zhang, Y.; Deng, Z.; Li, L.; Zhang, H. B.; Yu, Z. Z. Direct Ink Writing of Highly Conductive MXene Frames for Tunable Electromagnetic Interference Shielding and Electromagnetic Wave-Induced Thermochromism. *Nanomicro. Lett.* **2021**, *13*, 148.

(6) Song, P.; Liu, B.; Liang, C.; Ruan, K.; Qiu, H.; Ma, Z.; Guo, Y.; Gu, J. Lightweight, Flexible Cellulose-Derived Carbon Aerogel@ Reduced Graphene Oxide/PDMS Composites with Outstanding EMI Shielding Performances and Excellent Thermal Conductivities. *Nanomicro. Lett.* **2021**, *13*, 91.

(7) Qi, F.; Wang, L.; Zhang, Y.; Ma, Z.; Qiu, H.; Gu, J. Robust Ti3C2Tx MXene/starch derived carbon foam composites for superior EMI shielding and thermal insulation. *Mater. Today Phys.* **2021**, *21*, 100512.

(8) Zhang, Y.; Ruan, K.; Gu, J. Flexible Sandwich-Structured Electromagnetic Interference Shielding Nanocomposite Films with Excellent Thermal Conductivities. *Small* **2021**, *17*, 2101951.

(9) Arjmand, M.; Sundararaj, U. Electromagnetic interference shielding of Nitrogen-doped and Undoped carbon nanotube/polyvinylidene fluoride nanocomposites: A comparative study. *Compos. Sci. Technol.* **2015**, *118*, 257−263.

(10) Xu, Y. T.; Wang, Y.; Zhou, C. G.; Sun, W. J.; Dai, K.; Tang, J. H.; Lei, J.; Yan, D. X.; Li, Z. M. An electrically conductive polymer composite with a co-continuous segregated structure for enhanced mechanical performance. *J. Mater. Chem. C* **2020**, *8*, 11546−11554.

(11) Liang, C.; Gu, Z.; Zhang, Y.; Ma, Z.; Qiu, H.; Gu, J. Structural Design Strategies of Polymer Matrix Composites for Electromagnetic Interference Shielding: A Review. *Nanomicro. Lett.* **2021**, *13*, 181.

(12) Wu, H. Y.; Jia, L. C.; Yan, D. X.; Gao, J. F.; Zhang, X. P.; Ren, P. G.; Li, Z. M. Simultaneously improved electromagnetic interference shielding and mechanical performance of segregated carbon nanotube/polypropylene composite via solid phase molding. *Compos. Sci. Technol.* **2018**, *156*, 87−94.

(13) Wang, Y.; Fan, Z.-W.; Zhang, H.; Guo, J.; Yan, D. X.; Wang, S.; Dai, K.; Li, Z. M. 3D-printing of segregated carbon nanotube/polylactic acid composite with enhanced electromagnetic interference shielding and mechanical performance. *Mater. Des.* **2021**, *197*, 109222.

(14) Guan, X.; Zheng, G.; Dai, K.; Liu, C.; Yan, X.; Shen, C.; Guo, Z. Carbon Nanotubes-Adsorbed Electrospun PA66 Nanofiber Bundles with Improved Conductivity and Robust Flexibility. *ACS Appl. Mater. Interfaces* **2016**, *8*, 14150−14159.

(15) Zhang, X.; Lin, H.; Shang, H.; Xu, J.; Zhu, J.; Huang, W. Recent advances in functional fiber electronics. *SusMat* **2021**, *1*, 105−126.

(16) Arjmand, M.; Chizari, K.; Krause, B.; Pötschke, P.; Sundararaj, U. Effect of synthesis catalyst on structure of nitrogen-doped carbon nanotubes and electrical conductivity and electromagnetic interference shielding of their polymeric nanocomposites. *Carbon* **2016**, *98*, 358−372.

(17) Cai, J. H.; Tang, X. H.; Chen, X. D.; Wang, M. Temperature and strain-induced tunable electromagnetic interference shielding in polydimethylsiloxane/multi-walled carbon nanotube composites with temperature-sensitive microspheres. *Compos. Part A Appl. Sci. Manuf.* **2021**, *140*, 106188.

(18) Sun, R.; Zhang, H. B.; Liu, J.; Xie, X.; Yang, R.; Li, Y.; Hong, S.; Yu, Z. Z. Highly Conductive Transition Metal Carbide/Carbonitride-(MXene)@polystyrene Nanocomposites Fabricated by Electrostatic Assembly for Highly Efficient Electromagnetic Interference Shielding. *Adv. Funct. Mater.* **2017**, *27*, 1702807.

(19) Yu, W. C.; Zhang, G. Q.; Liu, Y. H.; Xu, L.; Yan, D. X.; Huang, H. D.; Tang, J. H.; Xu, J. Z.; Li, Z. M. Selective electromagnetic interference shielding performance and superior mechanical strength of conductive polymer composites with oriented segregated conductive networks. *Chem. Eng. J.* **2019**, *373*, 556−564.

(20) Kafle, A.; Luis, E.; Silwal, R.; Pan, H. M.; Shrestha, P. L.; Bastola, A. K. 3D/4D Printing of Polymers: Fused Deposition Modelling (FDM), Selective Laser Sintering (SLS), and Stereo-lithography (SLA). *Polymers* **2021**, *13*, 3101.

(21) Zhang, C.; Li, Y.; Kang, W.; Liu, X.; Wang, Q. Current advances and future perspectives of additive manufacturing for functional polymeric materials and devices. *SusMat* **2021**, *1*, 127−147.

(22) Jiang, Y.; Guo, F.; Liu, Y.; Xu, Z.; Gao, C. Three-dimensional printing of graphene-based materials for energy storage and conversion. *SusMat* **2021**, *1*, 304−323.

(23) Yuan, S.; Shen, F.; Chua, C. K.; Zhou, K. Polymeric composites for powder-based additive manufacturing: Materials and applications. *Prog. Polym. Sci.* **2019**, *91*, 141−168.

(24) Wu, H.; Fahy, W. P.; Kim, S.; Kim, H.; Zhao, N.; Pilato, L.; Kafi, A.; Bateman, S.; Koo, J. H. Recent developments in polymers/polymer nanocomposites for additive manufacturing. *Prog. Mater. Sci.* **2020**, *111*, 100638.

(25) Yuan, S.; Zheng, Y.; Chua, C. K.; Yan, Q.; Zhou, K. Electrical and thermal conductivities of MWCNT/polymer composites fabricated by selective laser sintering. *Compos. Part A Appl. Sci. Manuf.* **2018**, *105*, 203−213.

(26) Espera, A. H.; Valino, A. D.; Palaganas, J. O.; Souza, L.; Chen, Q.; Advincula, R. C. 3D Printing of a Robust Polyamide-12-Carbon Black Composite via Selective Laser Sintering: Thermal and Electrical Conductivity. *Macromol. Mater. Eng.* **2019**, *304*, 1800718.

(27) Cai, C.; Tey, W. S.; Chen, J.; Zhu, W.; Liu, X.; Liu, T.; Zhao, L.; Zhou, K. Comparative study on 3D printing of polyamide 12 by selective laser sintering and multi jet fusion. *J. Mater. Process. Technol.* **2021**, *288*, 116882.

(28) Mahmoodi, M.; Arjmand, M.; Sundararaj, U.; Park, S. The electrical conductivity and electromagnetic interference shielding of injection molded multi-walled carbon nanotube/polystyrene composites. *Carbon* **2012**, *50*, 1455−1464.

(29) Gan, X.; Wang, J.; Wang, Z.; Zheng, Z.; Lavorgna, M.; Ronca, A.; Fei, G.; Xia, H. Simultaneous realization of conductive segregation network microstructure and minimal surface porous macrostructure by SLS 3D printing. *Mater. Des.* **2019**, *178*, 107874.

(30) Song, S.; Li, Y.; Bai, S.; Wang, Q. Production of spherical polymeric composite powder for selective laser sintering via plasma assisted solid state shear milling: From theory to piezoelectric application. *Chem. Eng. J.* **2021**, *415*, 129035.

(31) Yang, L.; Wang, L.; Chen, Y. Solid-state shear milling method to prepare PA12/boron nitride thermal conductive composite powders and their selective laser sintering 3D-printing. *J. Appl. Polym. Sci.* **2019**, *137*, 48766.

(32) Jin, Y.; Chen, N.; Li, Y.; Wang, Q. The selective laser sintering of a polyamide 11/BaTiO$_3$/graphene ternary piezoelectric nanocomposite. *RSC Adv.* **2020**, *10*, 20405−20413.

(33) Liu, Y.; Zhang, B.; Xu, W.; Haibibu, A.; Han, Z.; Lu, W.; Bernholc, J.; Wang, Q. Chirality-induced relaxor properties in ferroelectric polymers. *Nat. Mater.* **2020**, *19*, 1169−1174.

(34) Liang, C.; Qiu, H.; Han, Y.; Gu, H.; Song, P.; Wang, L.; Kong, J.; Cao, D.; Gu, J. Superior electromagnetic interference shielding 3D graphene nanoplatelets/reduced graphene oxide foam/epoxy nanocomposites with high thermal conductivity. *J. Mater. Chem. C* **2019**, *7*, 2725−2733.

(35) Zhang, X. P.; Jia, L. C.; Zhang, G.; Yan, D. X.; Li, Z. M. A highly efficient and heat-resistant electromagnetic interference shielding carbon nanotube/poly(phenylene sulfide) composite via sinter molding. *J. Mater. Chem. C* **2018**, *6*, 10760−10766.

(36) Feng, D.; Xu, D.; Wang, Q.; Liu, P. Highly stretchable electromagnetic interference (EMI) shielding segregated polyurethane/carbon nanotube composites fabricated by microwave selective sintering. *J. Mater. Chem. C* **2019**, *7*, 7938−7946.

(37) Qing, Y.; Li, Y.; Luo, F. Electromagnetic interference shielding properties of nitrogen-doped graphene/epoxy composites. *J. Mater. Sci.: Mater. Electron.* **2020**, *32*, 25649−25655.

(38) Liu, D.-H.; Lai, Y.-S. Effectiveness of electromagnetic interference shielding of sputtered nitrogen-doped carbon thin films. *Diamond Relat. Mater.* **2021**, *111*, 108234.

(39) Sharif, F.; Arjmand, M.; Moud, A. A.; Sundararaj, U.; Roberts, E. P. L. Segregated Hybrid Poly(methyl methacrylate)/Graphene/Magnetite Nanocomposites for Electromagnetic Interference Shielding. *ACS Appl. Mater. Interfaces* **2017**, *9*, 14171−14179.

(40) Tang, X. H.; Tang, Y.; Wang, Y.; Weng, Y. X.; Wang, M. Interfacial metallization in segregated poly (lactic acid)/poly (ε-caprolactone)/multi-walled carbon nanotubes composites for enhancing electromagnetic interference shielding. *Compos. Part A Appl. Sci. Manuf.* **2020**, *139*, 106116.

(41) Hong, R.; Zhao, Z.; Leng, J.; Wu, J.; Zhang, J. Two-step approach based on selective laser sintering for high performance carbon black/ polyamide 12 composite with 3D segregated conductive network. *Composites, Part B* **2019**, *176*, 107214.

(42) Li, Z.; Wang, Z.; Gan, X.; Fu, D.; Fei, G.; Xia, H. Selective Laser Sintering 3D Printing: A Way to Construct 3D Electrically Conductive Segregated Network in Polymer Matrix. *Macromol. Mater. Eng.* **2017**, *302*, 1700211.

(43) Qi, F.; Chen, N.; Wang, Q. Preparation of PA11/BaTiO3 nanocomposite powders with improved processability, dielectric and piezoelectric properties for use in selective laser sintering. *Mater. Des.* **2017**, *131*, 135−143.

(44) Berretta, S.; Wang, Y.; Davies, R.; Ghita, O. R. Polymer viscosity, particle coalescence and mechanical performance in high-temperature laser sintering. *J. Mater. Sci.* **2016**, *51*, 4778−4794.

(45) Chatham, C. A.; Long, T. E.; Williams, C. B. A review of the process physics and material screening methods for polymer powder bed fusion additive manufacturing. *Prog. Polym. Sci.* **2019**, *93*, 68−95.

(46) Dowling, L.; Kennedy, J.; O'Shaughnessy, S.; Trimble, D. A review of critical repeatability and reproducibility issues in powder bed fusion. *Mater. Des.* **2020**, *186*, 108346.

(47) Riedlbauer, D.; Drexler, M.; Drummer, D.; Steinmann, P.; Mergheim, J. Modelling, simulation and experimental validation of heat transfer in selective laser melting of the polymeric material PA12. *Comput. Mater. Sci.* **2014**, *93*, 239−248.

(48) Abbasi, H.; Antunes, M.; Velasco, J. I. Recent advances in carbon-based polymer nanocomposites for electromagnetic interference shielding. *Prog. Polym. Sci.* **2019**, *103*, 319−373.

(49) Kumar, P.; Narayan Maiti, U.; Sikdar, A.; Kumar Das, T.; Kumar, A.; Sudarsan, V. Recent Advances in Polymer and Polymer Composites for Electromagnetic Interference Shielding: Review and Future Prospects. *Polym. Rev.* **2019**, *59*, 687−738.

(50) Yang, L.; Chen, Y.; Wang, M.; Shi, S.; Jing, J. Fused Deposition Modeling 3D Printing of Novel Poly(vinyl alcohol)/Graphene Nanocomposite with Enhanced Mechanical and Electromagnetic Interference Shielding Properties. *Ind. Eng. Chem. Res.* **2020**, *59*, 8066−8077.